THE EUROPEAN
PHYSICAL JOURNAL C

CrossMark

The limits on the strong Higgs sector parameters in the presence of new vector resonances

Mikuláš Gintner[1,2,a] , Josef Juráň[2,3,b]

[1] Physics Department, University of Zilina, Univerzitná 1, 010 26 Zilina, Slovakia
[2] Institute of Experimental and Applied Physics, Czech Technical University in Prague, Horská 3a/22, 128 00 Prague, Czech Republic
[3] Institute of Physics, Silesian University in Opava, Bezručovo nám. 13, 746 01 Opava, Czech Republic

Abstract In this paper, we investigate how the LHC data limit the Higgs-related couplings in the effective description of a strongly interacting extension of the Standard model. The Higgs boson is introduced as a scalar composite state and it is followed in the mass hierarchy by an $SU(2)$ triplet of vector composites. The limits are calculated from the constraints obtained in the recent ATLAS+CMS combined analysis of the data from 2011 and 2012. We find that the data prefer the scenario where the Higgs couplings to the electroweak gauge bosons differ from its couplings to the vector triplet. We also investigate the unitarity limits of the studied effective model for the experimentally preferred values of the Higgs couplings. We find from the $\pi\pi \rightarrow \pi\pi$ scattering amplitudes that for the vector resonance masses between one and two TeV significant portions of the experimentally allowed regions are well below the unitarity limit. We also evaluate how the existing ATLAS and CMS Run-2 data restrict our model with the upper bounds on the resonance production cross section times its branching ratio for various decay channels. The masses in the range 1 TeV $\leq M_\rho \leq$ 2 TeV are not excluded in parts or even full parameter space of our theory.

1 Introduction

Even though the LHC experiments ATLAS and CMS achieved a spectacular success by discovering the 125 GeV Higgs boson [1,2] it was more the beginning rather than the end of the struggle to uncover the character of physics beyond the Standard model (SM). To this moment, it has not even been settled down whether new physics takes the form of

weakly coupled supersymmetry or strongly coupled composites.

In the strongly coupled scenario, the observed lightness of the Higgs boson with respect to the expected size of the compositeness scale (naively, $\Lambda = 4\pi v \simeq 3$ TeV) could be explained if the Higgs boson were a (pseudo)Nambu–Goldstone boson after a breakdown of suitable extended global symmetry [3–10]. Another widely studied possibility is to embed the composite Higgs in an effective $SU(2)$ doublet [11–27] where its lightness would be guaranteed by the theory's particularities.

If the Higgs is generated as a composite state by new strong interactions the extension of the SM can be effectively described by higher dimensional operators that do not decouple in the low-energy limit. Presumably, they would modify the SM couplings of the Higgs boson with the heavy SM fields, such as the electroweak (EW) gauge bosons and/or the third quark generation. However, while the light SM Higgs boson can guarantee unitarity of the SM to virtually arbitrary high energies, this is not true anymore if the Higgs couplings become anomalous [28–30]. Nevertheless, the least one could require from the successful effective description of the composite state phenomenology is that it will not break down at energy below the compositeness scale. Meeting this expectation might be assisted with by the presence of additional new composite states which naturally occur in strongly interacting theories, anyway. Any further progress in dealing with these questions largely depends on an experimental input. Therefore, it is interesting to find what the most recent measurements of the Higgs boson couplings imply for various effective descriptions of strongly interacting extensions of the SM.

In this paper, we calculate the LHC limits on the effective theory describing possible early signs of strongly interacting physics beyond the SM. The effective description we work with is a rather simplistic view of what might be observed at

[a] e-mail: gintner@fyzika.uniza.sk
[b] e-mail: josef.juran@utef.cvut.cz

the LHC beyond the 125 GeV Higgs boson. We work with the vision where the Higgs boson is a scalar composite state followed in the mass hierarchy by a vector composite $SU(2)$ triplet state.Our approach is closely related to the formalism used in [31].

In particular, the Higgs sector of the effective Lagrangian under consideration is based on the non-linear sigma model with the 125-GeV $SU(2)_{L+R}$ scalar singlet complementing the non-linear triplet of the Nambu–Goldstone bosons. The new vector resonances are explicitly present in the form of an $SU(2)_{L+R}$ triplet. The vector triplet is introduced as a gauge field via the hidden local symmetry approach [32]. Consequently, it mixes with the EW gauge bosons. It results in the appearance of the mixing-generated (indirect) couplings of the vector triplet with all SM fermions. This setup fits the situation when the global $SU(2)_L \times SU(2)_R$ symmetry is broken down to $SU(2)_{L+R}$. The gauge sector of this effective description is equivalent to the gauge sector of highly deconstructed Higgsless model with only three sites [33].

The above-mentioned effective scenario has also been a basis for the effective Lagrangian we introduced and investigated in [34,35].[1] Therein, the vector triplet couples directly to the third quark doublet only and to none of the other SM fermions. In addition, even the interactions to the right quarks are not necessarily universal. Similar interaction patterns can be found in various recent extensions of the SM, including the partial compositeness and extra-dimensional scenarios. As was shown in [34,35] this arrangement helps relax the tight restrictions placed by the electroweak precision data on the vector triplet coupling to the light SM fermions, the bottom quark included. While the study in this paper follows our tBESS model (and, in the relevant parts, matches the model considered in [31]), its conclusions will also be partly, or fully, applicable to a wider class of effective models, e.g., with different fermionic sectors.

The question we address in this paper concerns a possible structure of the interactions between the new vector triplet and the Higgs boson. Under the considered symmetry, the Higgs boson coupling to the new vector triplet can differ from the Higgs couplings to the EW gauge bosons. This splitting might appear as an unwelcome complication. Nevertheless, as we will demonstrate in the paper, the ATLAS and CMS data support it. In particular, the $H \to \gamma\gamma$ constraint is the key component of the data that makes it difficult for the no-splitting scenario to satisfy the LHC measurements.

Using the results of [31,34,35] we also analyze the tree-level unitarity limits of our model resulting from the scattering of the longitudinal EW gauge bosons for the allowed values of the Higgs couplings obtained in this work. When

authors of [31] addressed unitarity questions the discovery of the Higgs boson was not confirmed yet. Thus, while they used the correct mass of the Higgs boson in their analysis, they were lacking any of the experimental input on the Higgs interactions available to us today. This was compensated for by the usage of the sum rules. However, one of the used sum rules imposes the no-spitting condition. The results of our analysis compel us to abandon this assumption and calculate the unitarity limits under different conditions.

This paper is organized as follows. In Sect. 2, we introduce the necessary components of the effective Lagrangian and work out the consequences of the Higgs-to-gauge-boson coupling splitting. Section 3 is devoted to the calculations of the constraints for the Higgs-to-gauge-boson couplings. Particularly, in Sect. 3.1, we set up the framework for the constraint calculations. In Sect. 3.2, we demonstrate the tension between the $H \to \gamma\gamma$ and other LHC measurement constraints for the model parameters when the universality of the Higgs-to-gauge-boson couplings is assumed. In Sect. 3.3, we calculate the best fits and constraints for the Higgs-to-gauge-boson parameters when the Higgs coupling to the new vector triplet can differ from the Higgs coupling to the EW gauge bosons. In Sect. 3.4 we investigate the unitarity limits for our model. Finally, in Sect. 4, we investigate the applicability of the existing LHC limits on the masses of new vector resonances to our model. We compare the predictions of our model for the production cross section of the vector resonance times its branching ratio for various decay channels with the existing experimental upper bounds obtained by the ATLAS and CMS Collaborations. Section 5 presents the conclusions of the paper.

2 The effective Lagrangian

The effective Lagrangian is built to respect the global $SU(2)_L \times SU(2)_R \times U(1)_{B-L} \times SU(2)_{HLS}$ symmetry of which the $SU(2)_L \times U(1)_Y \times SU(2)_{HLS}$ subgroup is also a local symmetry. The $SU(2)_{HLS}$ symmetry is an auxiliary gauge symmetry invoked to accommodate the $SU(2)$ triplet of vector resonances. Beside the scalar singlet $h(x)$ and the vector triplet $\mathbf{V}_\mu = (V_\mu^1, V_\mu^2, V_\mu^3)$, the effective Lagrangian is built out of the SM fields only.

The Lagrangian can be split in three terms[2]

$$\mathcal{L} = \mathcal{L}_{\text{GB}} + \mathcal{L}_{\text{ESB}} + \mathcal{L}_{\text{ferm}}, \qquad (1)$$

where $\mathcal{L}_{\text{GB}}$ describes the gauge-boson sector including the $SU(2)_{\text{HLS}}$ triplet,

---

[1] We call it the tBESS model to stress its connection to the BESS model [36–38]. The name modifying "t" suggests a special standing of the top-quark related doublet in the model.

[2] While the full formulation of the model can be found in [35], the definitions of basic quantities used in Eqs. (2) through (5) are, for the reader's convenience, summarized in Appendix.

$$\mathcal{L}_{\text{GB}} = \frac{1}{2g^2}\text{Tr}(\boldsymbol{W}_{\mu\nu}\boldsymbol{W}^{\mu\nu}) + \frac{1}{2g'^2}\text{Tr}(\boldsymbol{B}_{\mu\nu}\boldsymbol{B}^{\mu\nu})$$
$$+ \frac{2}{g''^2}\text{Tr}(\boldsymbol{V}_{\mu\nu}\boldsymbol{V}^{\mu\nu}), \tag{2}$$

$\mathcal{L}_{\text{ESB}}$ is the scalar sector responsible for spontaneous breaking of the electroweak and hidden local symmetries, and $\mathcal{L}_{\text{ferm}}$ is the fermion Lagrangian of the model.

Let us express $\mathcal{L}_{\text{ESB}}$ as a sum of two terms, $\mathcal{L}_{\text{ESB}} = \mathcal{L}_h + \mathcal{L}_{\text{hV}}$, where

$$\mathcal{L}_h = \frac{1}{2}\partial_\mu h \partial^\mu h - \frac{1}{2}M_h^2 h^2 - c_h \frac{M_h^2}{2v}h^3 - c_h'\frac{M_h^2}{8v^2}h^4 \tag{3}$$

contains the kinetic term and the self-interactions of the Higgs boson with the mass $M_h = 125$ GeV and free parameters c_h and c_h'. Furhter,

$$\mathcal{L}_{\text{hV}} = -v^2\left[\text{Tr}(\bar{\omega}^\perp)^2\left(1 + 2a_V\frac{h}{v} + a_V'\frac{h^2}{v^2} + \dots\right)\right.$$
$$\left. -v^2 + \alpha\text{Tr}(\bar{\omega}^\parallel)^2\left(1 + 2a_\rho\frac{h}{v} + a_\rho'\frac{h^2}{v^2} + \dots\right)\right] \tag{4}$$

is responsible for the masses of all gauge bosons including the new vector triplet, and describes their interactions with the Higgs boson. The interactions are parameterized by the free parameters $a_V, a_\rho, a_V', a_\rho', \dots$. Below, only the interaction terms of (4) that are at most linear in h will be considered.[3] Terms with higher powers of h, which are not important for higgs phenomenology at the LHC, can be restored at any time without affecting our conclusions.

The fermion sector $\mathcal{L}_{\text{ferm}}$ in its minimal formulation contains the fermionic kinetic terms and the fermion interactions with the EW gauge bosons as well as terms responsible for the couplings of the SM fermions to the Higgs boson. While the EW part is kept identical to the SM one, the interactions of the Higgs boson with the fermions can assume non-SM values. Their parameterization is based on the following interaction Lagrangian:

$$\mathcal{L}_{\text{ferm}}^{\text{scalar}} = -\sum_{k=1}^{6}\bar{\psi}_L^k U M_f^k\left(1 + c_f^k\frac{h}{v} + c_f'^k\frac{h^2}{v^2} + \dots\right)\psi_R^k + \text{h.c.}, \tag{5}$$

where M_f^k is a 2×2 diagonal matrix with the masses of the upper and bottom k^{th} fermion doublet components on its diagonal, and $U = \xi(\pi)\cdot\xi(\pi) = \exp(2i\pi\tau/v)$. Note that when $c_k = 1, \forall k$, and the rest of c's are zeros the scalar resonance interactions with fermions imitate the corresponding

interactions of the SM Higgs boson. Again, only the interaction terms that are at most linear in h will be considered below.

Possible direct interactions of the fermions with the vector triplet do not play a role in the calculation of the limits investigated in this paper. Thus, this part of the effective Lagrangian is left unspecified. Nevertheless, we would like to mention the example of the setup of this sector where only the third quark generation couples directly to the vector triplet and the interaction of the right top quark is disentangled from the interaction of the right bottom quark. We suggested and analyzed the effective model with this kind of the fermion sector in [34,35]. For the sake of completeness, we would like to point out that in this model the vector resonances do interact with the SM fermions, including the light ones, even if there are no direct interactions introduced. This is due to the mixing between the EW gauge bosons and the vector resonance triplet. Of course, the mixing-induced couplings are suppressed by the transformation matrix elements; they are proportional to $1/g''$.

The mixing of the gauge fields occurs in the process of diagonalization of the gauge-boson mass matrix. After gauging out all six Goldstone bosons the Lagrangian $\mathcal{L}_{\text{hV}}$ reads

$$\mathcal{L}_{\text{hV}} = \mathcal{M}(\alpha) + \frac{2a_V}{v}\mathcal{M}(\alpha r)h, \tag{6}$$

where $r = a_\rho/a_V$ and where

$$\mathcal{M}(\alpha) \equiv \frac{1}{2}(X_\mu^-)^\dagger\cdot\boldsymbol{M}_{\mathbf{C}}^2(\alpha)\cdot X_\mu^- + \frac{1}{2}(X_\mu^+)^\dagger\cdot\boldsymbol{M}_{\mathbf{C}}^2(\alpha)\cdot X_\mu^+$$
$$+ \frac{1}{2}(X_\mu^0)^\dagger\cdot\boldsymbol{M}_{\mathbf{N}}^2(\alpha)\cdot X_\mu^0 \tag{7}$$

is the gauge-boson mass term. Further, $X^\pm = (W_f^\pm, V^\pm)^T$, $X^0 = (W^3, B, V^3)^T$, and $\boldsymbol{M}_{\mathbf{C}}^2(\alpha)$ and $\boldsymbol{M}_{\mathbf{N}}^2(\alpha)$ are the squared-mass matrices of the charged and neutral gauge bosons, respectively,

$$\boldsymbol{M}_{\mathbf{C}}^2 = \frac{v^2}{4}\begin{pmatrix}(1+\alpha)g^2 & -\alpha gg'' \\ -\alpha gg'' & \alpha g''^2\end{pmatrix}, \tag{8}$$

$$\boldsymbol{M}_{\mathbf{N}}^2 = \frac{v^2}{4}\begin{pmatrix}(1+\alpha)g^2 & -(1-\alpha)gg' & -\alpha gg'' \\ -(1-\alpha)gg' & (1+\alpha)g'^2 & -\alpha g'g'' \\ -\alpha gg'' & -\alpha g'g'' & \alpha g''^2\end{pmatrix}. \tag{9}$$

The diagonalization process results in the transformation of the gauge-boson basis, from the mass one to the flavor one, $\{Y\}\to\{X\}$:

$$X_\mu^\pm = O^{(C)}\cdot Y_\mu^\pm, \qquad X_\mu^0 = O^{(N)}\cdot Y_\mu^0, \tag{10}$$

where $Y^\pm = (W_m^\pm, \rho^\pm)^T$, $Y^0 = (A, Z, \rho^0)^T$. Note that we use V_μ^a to denote the vector resonance components in the

---

[3] Although the quadratic terms would be needed if one wished to maintain the possibility to eliminate the linear growth in s from the scattering amplitude $\pi\pi\to hh$ and thus improve the unitarity limit for the model.

flavor basis and ρ_μ^a for the vector resonance components in the mass basis.[4]

In the limit $M_{W^\pm}, M_Z \ll M_{\rho^0}$, equivalent to the condition $g, G \ll \sqrt{\alpha} g''$, the mixing matrices read

$$O^{(C)} = \begin{pmatrix} 1 & -g/g'' \\ g/g'' & 1 \end{pmatrix}, \quad (11)$$

$$O^{(N)} = \begin{pmatrix} g'/G & g/G & -g/g'' \\ g/G & -g'/G & -g'/g'' \\ 2\frac{gg'}{Gg''} & \frac{g^2-g'^2}{Gg''} & 1 \end{pmatrix}. \quad (12)$$

In the same limit, the next-to-leading order approximations of the gauge-boson masses read

$$M_{W^\pm} = \frac{vg}{2}\left(1 - \frac{g^2}{2g''^2}\right), \quad (13)$$

$$M_{\rho^\pm} = \frac{\sqrt{\alpha} v g''}{2}\left(1 + \frac{g^2}{2g''^2}\right), \quad (14)$$

and

$$M_Z = \frac{vG}{2}\left[1 - \frac{(g^2-g'^2)^2}{2g''^2 G^2}\right], \quad (15)$$

$$M_{\rho^0} = \frac{\sqrt{\alpha} v g''}{2}\left(1 + \frac{G^2}{2g''^2}\right). \quad (16)$$

The leading order approximation for the partial width of the ρ decay to the EW gauge bosons is

$$\Gamma(\rho^0 \to W^+ W^-) = \Gamma(\rho^\pm \to W^\pm Z) = \frac{M_\rho^5}{48\pi v^4 g''^2}. \quad (17)$$

The interactions of the gauge bosons with the Higgs can be read off from $\mathcal{L}_{hV}$ in the mass basis

$$\frac{2a_V}{v}\mathcal{M}(\alpha r)h = \frac{2h}{v}\Bigg[\frac{1}{2}c_Z M_Z^2 Z_\mu Z^\mu + c_W M_W^2 W_\mu^+ W^{-\mu}$$

$$+ \frac{1}{2}c_{\rho^0}M_{\rho^0}^2 \rho_\mu^0 \rho^{0\mu} + c_{\rho^\pm}M_{\rho^\pm}^2 \rho_\mu^+ \rho^{-\mu}$$

$$+ c_{W\rho^\pm}M_W M_{\rho^\pm}(W_\mu^+ \rho^{-\mu} + \text{h.c.})$$

$$+ c_{Z\rho^0}M_Z M_{\rho^0} Z_\mu \rho^{0\mu}\Bigg] \quad (18)$$

with the anomalousness factors[5] $c_{YY'}$. If the flavor basis splitting factor r equals 1 ($a_\rho = a_V$) then the mass basis couplings $c_{YY'}$ follow a simple pattern

$$c_Z = c_W = c_{\rho^0} = c_{\rho^\pm} = a_V, c_{Z\rho^0} = c_{W\rho^\pm} = 0. \quad (19)$$

---

[4] We also used the subscripts m and f to distinguish the components of $W^\pm$ fields in the two bases. We do not use the subscripts if the choice of the basis is obvious from the context.

[5] If $Y = Y'$ then a single letter subscript will be used, e.g. $c_{YY} \to c_Y$.
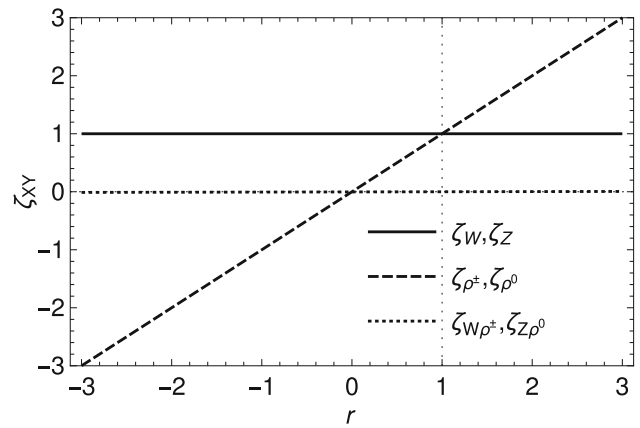
Fig. 1 The mass basis splitting factors ζ_{XY} as functions of the splitting $r = a_\rho/a_V$. The graphs are plotted for $M_{\rho^0} = 1.5$ TeV and $g'' = 15$

For a more general situation, $a_\rho \neq a_V$, the relations of $c_{YY'}$'s to a_V and a_ρ become more intricate. Let us introduce the mass basis splitting factors $\zeta_{YY'}$ such that

$$c_{YY'} = a_V \zeta_{YY'}. \quad (20)$$

Then

$$\zeta_{YY'}(\alpha, r) = \frac{O_{Y_1 Y}(\alpha) \cdot [M_{\mathbf{C},\mathbf{N}}^2(\alpha r)]_{Y_1 Y_2} \cdot O_{Y_2 Y'}(\alpha)}{M_Y(\alpha) M_{Y'}(\alpha)} \quad (21)$$

The $\zeta_{YY'}$ factors for the individual gauge bosons are summarized in Table 1. There, we have introduced auxiliary variables

$$\sqrt{D_N} = \frac{4}{v^2}\left(M_{\rho^0}^2 - M_Z^2\right), \quad (22)$$

$$\sqrt{D_C} = \frac{4}{v^2}\left(M_{\rho^\pm}^2 - M_W^2\right), \quad (23)$$

and

$$k_N = [1 - 4\alpha(g^2 - g'^2)^2/D_N]^{1/2}, \quad (24)$$

$$k_C = (1 - 4\alpha g^4/D_C)^{1/2}. \quad (25)$$

Note that $k_{N,C} = 1 - \mathcal{O}(x^4)$ where $x = g/(\sqrt{\alpha}g'') \approx M_W/M_\rho$.

Figure 1 helps to understand how the flavor basis splitting, $r = a_\rho/a_V$, translates into the anomalous factors $c_{YY'}$. The essential role in this issue is played by the ζ factors. Therefore, the graphs in the figure depict the dependences of ζ's on r. There, the plots of $\zeta_{W,Z}$ are almost perfect horizontal lines at 1 which complies with $\zeta_{W,Z} = 1 - (1 - r)\mathcal{O}(x^4)$. On the other hand, $\zeta_{\rho^\pm,\rho^0} = r + (1 - r)\mathcal{O}(x^4)$ suggests the straight line of the 45 degree slope for $\zeta_{\rho^\pm,\rho^0}(r)$. Finally, the ζ factors of the mixed interaction terms are negligible when compared to the other ζ's, which is in agreement with the finding that $\zeta_{W\rho^\pm, Z\rho^0} = (1 - r)\mathcal{O}(x^2)$.

While all ζ's depend on g'' and M_ρ these dependences are very weak. When changing (g'', M_ρ) from (10, 1 TeV)

Table 1 The mass basis splitting factors $\zeta_{YY'}(\alpha, r)$ for the individual gauge bosons Y, $Y' \in \{W^\pm, \rho^\pm, A, Z, \rho^0\}$

$\zeta_{YY'}(\alpha, r)$	ρ^0	Z	A	$\rho^\pm$	$W^\pm$
$W^\pm$	0	0	0	$g^2\sqrt{\frac{\alpha}{D_C}}(r-1)$	$\frac{1+r+(1-r)k_C}{2}$
$\rho^\pm$	0	0	0	$\frac{1+r-(1-r)k_C}{2}$	
A	0	0	0		
Z	$(g^2 - g'^2)\sqrt{\frac{\alpha}{D_N}}(r-1)$	$\frac{1+r+(1-r)k_N}{2}$			
ρ^0	$\frac{1+r-(1-r)k_N}{2}$				
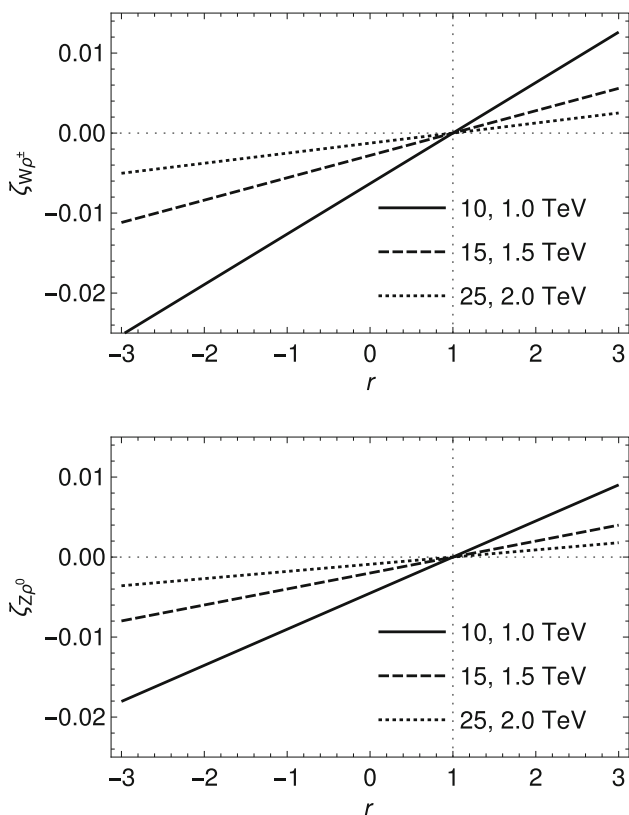
Fig. 2 The non-diagonal splitting factors $\zeta_{W\rho^\pm}$ (*left panel*) and $\zeta_{Z\rho^0}$ (*right panel*) as functions of the splitting $r = a_\rho/a_V$. The *solid lines* correspond to $(g'', M_\rho) = (10, 1 \text{ TeV})$, the *dashed lines* to $(15, 1.5 \text{ TeV})$, and the *dotted lines* to $(25, 2 \text{ TeV})$

to $(25, 2 \text{ TeV})$, ζ_W and ζ_Z vary no more than by about 10^{-4} for $-3 \leq r \leq 3$. The same conclusion applies to $\zeta_{\rho^\pm}$ and ζ_{ρ^0}. The actual size of $\zeta_{W\rho^\pm}$ and $\zeta_{Z\rho^0}$ as well as their dependence on g'' and M_ρ can be seen in Fig. 2. Consequently, for many phenomenological considerations the relations

$$c_Z = c_W = a_V, \quad c_{\rho^0} = c_{\rho^\pm} = a_\rho = ra_V,$$
$$c_{Z\rho^0} = c_{W\rho^\pm} = 0,$$ (26)

represent satisfactory approximations over quite a large region of r values and for all relevant values of g'' and M_ρ.

Now, let us turn our attention to the Higgs-to-gauge-boson couplings. Beside being proportional to the splitting factors

the couplings are amplified by the (squares of) gauge-boson masses. Namely,

$$g_{hWW} = a_V \zeta_W M_W^2, \quad g_{hZZ} = a_V \zeta_Z M_Z^2/2,$$ (27)

$$g_{h\rho^+\rho^-} = a_V \zeta_{\rho^\pm} M_{\rho^\pm}^2, \quad g_{h\rho^0\rho^0} = a_V \zeta_{\rho^0} M_{\rho^0}^2/2,$$ (28)

$$g_{hW\rho^\pm} = a_V \zeta_{W\rho^\pm} M_W M_{\rho^\pm}, \quad g_{hZ\rho^0} = a_V \zeta_{Z\rho^0} M_Z M_{\rho^0}.$$ (29)

Then

$$\frac{g_{hWW}}{g_{hZZ}} = 2\frac{\zeta_W}{\zeta_Z}\frac{M_W^2}{M_Z^2} = 2[1 + (r-1)\,\mathcal{O}(x^4)]\frac{M_W^2}{M_Z^2}.$$ (30)

Here, the whole dependence on new physics is contained in the $\mathcal{O}(x^4)$ term. Thus, the splitting can modify the SM expectation for the ratio (30) only very slightly. On the other hand, owing to the new vector triplet's large mass new physics becomes manifest the most in the Higgs interaction with the new vector triplet as can be seen in

$$\frac{g_{h\rho^+\rho^-}}{g_{hWW}} = \frac{\zeta_{\rho^\pm}}{\zeta_W}\frac{M_{\rho^\pm}^2}{M_W^2} \approx r\,\frac{M_{\rho^\pm}^2}{M_W^2},$$ (31)

$$\frac{g_{h\rho^0\rho^0}}{g_{hZZ}} = \frac{\zeta_{\rho^0}}{\zeta_Z}\frac{M_{\rho^0}^2}{M_Z^2} \approx r\,\frac{M_{\rho^0}^2}{M_Z^2}.$$ (32)

Note that while the vector mass affects the ratios significantly their dependences on g'' are completely ignorable. In Fig. 3, the ratios $g_{h\rho^+\rho^-}/g_{hWW}$ and $g_{h\rho^0\rho^0}/g_{hZZ}$ as functions of r and for various vector resonance masses are depicted.

If the splitting takes place new physics also manifests via the emergence of two new vertices, $hW^\pm\rho^\pm$ and $hZ\rho^0$, not present either in the SM or in the Lagrangian $\mathcal{L}_{hV}$ when $a_\rho = a_V$. Even though the new coupling strengths lag far behind the strengths of the $h\rho^+\rho^-$ and $h\rho^0\rho^0$ couplings their presence would introduce new phenomena. The relative strengths of the $hW^\pm\rho^\pm$ and $hZ\rho^0$ couplings with respect to the hWW and hZZ couplings, respectively, are given by
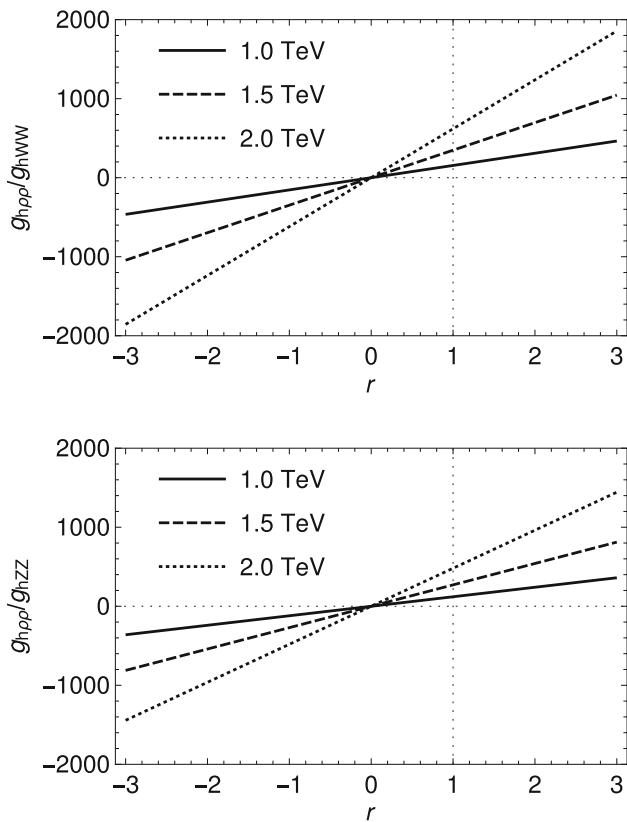
Fig. 3 The relative strengths of the $h\rho^+\rho^-$ and $h\rho^0\rho^0$ couplings with respect to the hW^+W^- and hZZ couplings, respectively, as functions of the splitting $r = a_\rho/a_V$. The *solid lines* correspond to $M_\rho = 1$ TeV, the *dashed lines* to 1.5 TeV, and the *dotted lines* to 2 TeV

Fig. 4 The relative strengths of the $hW\rho^\pm$ and $hZ\rho^0$ couplings with respect to the hW^+W^- and hZZ couplings, respectively, as functions of the splitting $r = a_\rho/a_V$. The *solid lines* correspond to $g'' = 10$, the *dashed lines* to $g'' = 15$, and the *dotted lines* to $g'' = 25$

$$\frac{g_{hW\rho}}{g_{hWW}} = \frac{\zeta_{W\rho}}{\zeta_W}\frac{M_{\rho^\pm}}{M_W} = (r-1)\,\mathcal{O}(x), \tag{33}$$
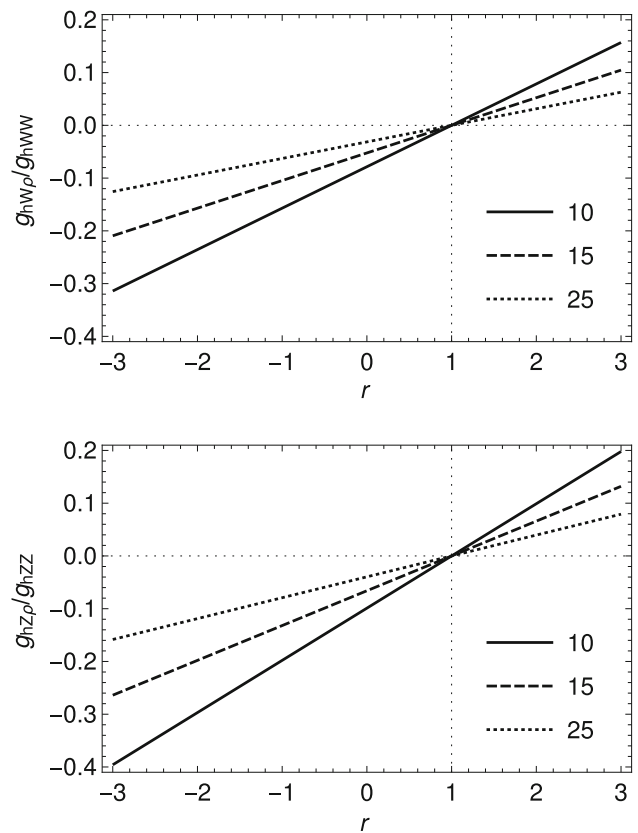
$$\frac{g_{hZ\rho}}{g_{hZZ}} = 2\frac{\zeta_{Z\rho}}{\zeta_Z}\frac{M_{\rho^0}}{M_Z} = (r-1)\,\mathcal{O}(x). \tag{34}$$

Note that while these ratios are affected significantly by g'' their dependences on the vector mass are completely ignorable. In Fig. 4, the ratios $g_{hW\rho^\pm}/g_{hWW}$ and $g_{hZ\rho^0}/g_{hZZ}$ as functions of r and for various g'' values are depicted.

The splitting of a_ρ from a_V will also cause $c_W \neq c_Z$. Thus, in principle, r affects the model prediction for the custodial symmetry protected rho parameter. Fortunately, the effect is negligible for a wide range of r values. To demonstrate it we inspect the prediction for the ratio $\lambda_{WZ} \equiv c_W/c_Z$

$$\lambda_{WZ} = \frac{\zeta_W}{\zeta_Z} = 1 + (r-1)\,\mathcal{O}(x^4). \tag{35}$$

Numerically, our model predicts $|\lambda_{WZ} - 1| < 6 \times 10^{-5}$ at tree level when $-3 \leq r \leq 3$, $10 \leq g'' \leq 25$, and $M_\rho \in (1, 2)$ TeV. The current experimental limit is $\lambda_{WZ} = 0.88^{+0.10}_{-0.09}$ [39].

3 Limits on the Higgs-related parameters

3.1 Relevant measurements

In this paper, we would like to identify the restrictions that the current LHC measurements provide for the free parameters of the effective Lagrangian under consideration. While the LHC cannot compete yet with the low-energy data from the LEP, SLC, and Tevatron in setting a limit on the value of g'', it certainly plays the key role in restricting the Higgs-related couplings of the EW gauge bosons, fermions, and the vector resonance.

In [35], we calculated the indirect limits on g'' and other free parameters of the tBESS phenomenological Lagrangian, a special case of the Lagrangian considered here, fitting the observables $\epsilon_1, \epsilon_2, \epsilon_3, \Gamma_b(Z \to b\bar{b}+X)$, and BR($B \to X_s\gamma$) under the assumption $a_V = a_\rho = 1$ and $M_\rho = 1$ TeV and 2 TeV. In addition to the setup investigated here, the tBESS model contains three independent direct interactions of the vector triplet with fermions: one with the left top-

bottom quark doublet, another with the right top quark, and yet another with the right bottom quark. The analysis of the limits lead to the conclusion about the preference of higher g'' values, namely $g'' > 12$ at 95% CL when combined with preferred values of other free parameters. Further, the analysis seemed to support the assumption of some models of partial fermion compositeness that the new strong physics resonances couple stronger to the right top quark than to the right bottom quark.

The requirement that our Lagrangian be treatable perturbatively bounds the values of g'' from above by the naive perturbativity limit, $g''/2 \overset{<}{\sim} 4\pi$, implying $g'' \overset{<}{\sim} 25$. If we took this value as the final say in this issue it would not be reasonable to use g'' higher than about 20 in our calculations. However, one can imagine that a more rigorous analysis of the perturbativity limit could somehow modify its value one way or the other.

The limits on the Higgs-related couplings of the studied Lagrangian can be obtained from the existing measurements of the LHC experiments. In this paper, we use constraints from the ATLAS+CMS Collaborations analysis [39] based on the combination of six decay channels, namely $H \rightarrow \gamma\gamma$, $ZZ^*, WW^*, b\bar{b}, \tau\bar{\tau}$ and $\mu\bar{\mu}$, and of five production processes, namely gluon and vector boson fusions, and associated productions with W, Z, or a pair of top quarks. In our analysis, we assume that there is only one SM-like Higgs boson state at about 125 GeV of a negligible decay width.

3.1.1 The interim framework

In [39], the combined ATLAS and CMS measurements were utilized to calculate fits and limits on the free kappa parameters of the interim framework introduced in [40]. In this framework, kappas parameterize possible deviations of the Higgs interactions from their SM expectations. The kappas are introduced so that the squared free parameters κ_i scale the SM Higgs production cross sections σ_i^{SM} and/or the partial Higgs decay widths Γ_i^{SM} associated with the ith SM particle. When $\kappa_i = 1$ then the best available SM predictions for $\sigma_i \cdot \mathrm{BR}_i$ are recovered so that for the true SM Higgs boson no artificial deviations caused by ignored higher-order corrections are present.

The particular interim framework scenario that suits our effective Lagrangian is that of Section 6.1 of [39]. In this scenario, it is assumed that there are no non-SM decays of the Higgs and that the branching ratio of invisible and/or undetected decay products is zero. New particles in loops are allowed. Assuming that $\kappa_c = \kappa_t$, $\kappa_s = \kappa_b$, and $\kappa_\mu = \kappa_\tau$ there are generally seven free parameters in this scenario: five tree-level kappas ($\kappa_W, \kappa_Z, \kappa_t, \kappa_b, \kappa_\tau$) and two loop-level kappas (κ_g and κ_γ). The loop-level kappas are associated with the higher-order effective vertices Hgg and $H\gamma\gamma$.

Table 2 The experimental limits for κ's that will be fitted to find the restrictions and the best values of a_V, a_ρ, and c_t. Note that the kappa limits were obtained under the assumption that $\kappa_t > 0$

Parameter	ATLAS + CMS Limits
κ_W	0.87 ± 0.13
κ_Z	-0.98 ± 0.10
κ_t	1.40 ± 0.24
$|\kappa_\gamma|$	0.87 ± 0.14
$|\kappa_g|$	0.78 ± 0.13

We will derive the limits on a_V, a_ρ, and c_t fitting the experimental values of kappas from Table 17 of [39] (the $B_{\mathrm{BSM}} = 0$ part). The kappa values were obtained assuming $\kappa_t > 0$ and using the following input parameters for the calculation of the SM quantities[6] [41]: $M_W = 80.398$ GeV, $M_Z = 91.1876$ GeV, $G_F = 1.16637 \times 10^{-5}$ GeV^{-2}, $M_t = 172.5$ GeV, $M_h = 125.5$ GeV. There are five kappas relevant for calculations of our limits: $\kappa_\gamma, \kappa_W, \kappa_Z, \kappa_g$, and κ_t. The remaining kappas, κ_b and κ_τ do not depend on a_V, a_ρ, or c_t, at leading order.

The experimental uncertainties on kappas quoted in [39] are asymmetric. In our analysis, we will simplify the situation by equalizing both sides of the uncertainty to the one that is bigger. In addition, the 1-sigma interval of κ_Z consists of two disconnected regions. In this case, we take into account only the region where the best-fit value of κ_Z is placed. Thus modified experimental limits on κ's that will be used in our calculations are shown in Table 2.

3.1.2 Fitting kappas with the effective Lagrangian parameters

To restrict the free Higgs parameters via the fit to kappas the relations between the related kappas and c_i's have to be established. For that purpose we use some of the kappa defining quantities utilized in fitting the experiment and equate them to the predictions of our effective theory. With the input parameters listed above we obtain

$$\kappa_W^2 \equiv \frac{\Gamma_{WW^*}}{\Gamma_{WW^*}^{\mathrm{SM}}} = c_W^2, \quad \kappa_Z^2 \equiv \frac{\Gamma_{ZZ^*}}{\Gamma_{ZZ^*}^{\mathrm{SM}}} = c_Z^2,$$

$$\kappa_t^2 \equiv \frac{\sigma_{t\bar{t}H}}{\sigma_{t\bar{t}H}^{\mathrm{SM}}} = c_t^2, \quad \kappa_g^2 \equiv \frac{\sigma_{\mathrm{ggF}}}{\sigma_{\mathrm{ggF}}^{\mathrm{SM}}} = c_t^2, \tag{36}$$

where $\sigma_{t\bar{t}H}$ is the cross section of associated production of the Higgs boson with a pair of top quarks, σ_{ggF} is the gluon-fusion Higgs production cross section, and Γ_{jj}'s are the partial Higgs decay widths to the dibosons, $jj = WW^*, ZZ^*$. The index "SM" denotes the SM values.

---

[6] Here we quote only the values of those input quantities that will also be needed as inputs in the calculations in this paper.

As is well known, the $H \rightarrow \gamma\gamma$ decay in the SM occurs at the loop level only. In the SM, two dominant contributions originate from the Feynman diagrams with the W boson and top quark loops. Beyond the SM the anomalous couplings of the Higgs boson to W and top quark are parameterized by the factors c_W and c_t, respectively. In addition, the $H \rightarrow \gamma\gamma$ decay can be modified by the extra diagram with the $\rho^\pm$ resonance in the loop. Thus, our effective theory predicts

$$\kappa_\gamma^2 \equiv \frac{\Gamma_{\gamma\gamma}}{\Gamma_{\gamma\gamma}^{\mathrm{SM}}} = \left[\frac{\alpha_{\mathrm{EM}}(g'', M_\rho)}{\alpha_{\mathrm{EM}}^{\mathrm{SM}}}\right]^2 \left[\frac{c_\gamma(c_W, c_t, c_{\rho^\pm})}{c_\gamma^{\mathrm{SM}}}\right]^2,$$
(37)

where c_γ^{SM} is the SM coupling of the $H\gamma\gamma$ effective vertex and $c_\gamma(c_W, c_t, c_{\rho^\pm})$ is its anomalous analog. Further, α_{EM} is the electromagnetic coupling constant which, in the case of the effective Lagrangian and for the given set of the input parameters [41], depends on new physics. The leading order approximation that dominates the ratio of the squared α_{EM}'s when $M_\rho \gg M_Z$ reads

$$\frac{\alpha_{\mathrm{EM}}^2(g'')}{(\alpha_{\mathrm{EM}}^{\mathrm{SM}})^2} = \frac{1}{\left[1 + 16\sqrt{2}G_F M_W^2 (1 - M_W^2/M_Z^2)/g''^2\right]^2}.$$
(38)

Numerically, when g'' varies between 10 and 25 then $(\alpha_{\mathrm{EM}}/\alpha_{\mathrm{EM}}^{\mathrm{SM}})^2$ changes from 0.992 to 0.999. Thus, this effect will be ignored in our further analysis. Also, note that in the leading order the ratio is not affected by the mass of the vector resonance.

The contribution of the $\rho^\pm$ resonance to $h \rightarrow \gamma\gamma$ mimics the contribution of $W^\pm$; the only difference comes from different masses and couplings of the vector particles. Thus, considering the principal contributions only—from the top, W, and ρ loops—c_γ reads

$$c_\gamma = \frac{1}{8}\left[c_t N_C q_t^2 F_{\mathrm{ferm}}(x_t) + c_W F_{\mathrm{vec}}(x_W)\right.$$
$$\left. + c_{\rho^\pm} F_{\mathrm{vec}}(x_\rho)\right],$$
(39)

where $N_C q_t^2 = 4/3$, $x_i = 4M_i^2/M_h^2$, and

$$F_{\mathrm{ferm}}(x) = -2x[1 + (1 - x)f(x)],$$
(40)
$$F_{\mathrm{vec}}(x) = 2 + 3x + 3x(2 - x)f(x),$$
(41)

where

$$f(x) = \begin{cases} \arcsin^2(1/\sqrt{x}), & x \geq 1, \\ -\frac{1}{4}\left[\ln\left(\frac{1+\sqrt{1-x}}{1-\sqrt{1-x}}\right) - i\pi\right]^2, & x < 1. \end{cases}$$
(42)

For the given input values we get $F_{\mathrm{ferm}}(x_t) = -1.38$, $F_{\mathrm{vec}}(x_W) = 8.34$, $F_{\mathrm{vec}}(x_{1\mathrm{TeV}}) = 7.01$, and $F_{\mathrm{vec}}(x_{2\mathrm{TeV}}) = 7.00$. Then

$$c_\gamma(M_\rho = 1\text{–}2\,\mathrm{TeV}) = -0.23\,c_t + 1.04\,c_W + 0.88\,c_{\rho^\pm}$$
$$= -0.23\,c_t + a_V\,[1.04\,\zeta_W(r)$$
$$+ 0.88\,\zeta_{\rho^\pm}(r)].$$
(43)

Note that, for the displayed decimal places, the numerical coefficients in this formula are not sensitive to varying the ρ mass between 1 and 2 TeV.

The SM value of c_γ is obtained when $c_t = c_W = 1$ and $c_{\rho^\pm} = 0$: $c_\gamma^{\mathrm{SM}} = 0.81$.

The effective Lagrangian predictions for observables do not change under the simultaneous sign change of all c_i parameters. Therefore, a sign of one of c_i's can be fixed without losing physically distinguishable configurations of theory. Owing to that we choose $c_t > 0$ throughout the paper.

3.2 Failure of the $a_V = a_\rho$ scenario

Before performing the full fit on $\kappa_\gamma, \kappa_W, \kappa_Z, \kappa_g$, and κ_t with three free parameters a_V, a_ρ, c_t let us provide a simple demonstration that the no-splitting scenario, $a_V = a_\rho$, has a hard time to satisfy the experimental restrictions on the kappas under consideration. Applying (37) to this situation we obtain

$$|\kappa_\gamma| = |2.37\,a_V - 0.28\,c_t|.$$
(44)

Using the experimental restriction on κ_γ (see Table 2) the Eq. (44) results in the allowed region comprised of two parallel stripes crossing the $a_V - c_t$ plane as shown in Fig. 5. Let us recall that we work under the assumption $c_t > 0$ which reduces the $a_V - c_t$ plane to a half-plane.

In addition, the graphs in Fig. 5 display rectangular intersections of the experimentally allowed regions for a_V and c_t. The limit on a_V is derived by fitting κ_W^2 and κ_Z^2 while taking into account the no-splitting relations $c_W = c_Z = a_V$. The relevant χ^2-function consists of the last two terms of (46). The obtained fit reads $|a_V| = 0.93 \pm 0.08$ where the absolute value originate in the fitting of squares of variables. Analogically, the c_t constraint is obtained by fitting κ_t^2 and κ_g^2. The corresponding χ^2-function contains the second and third terms of (46). The obtained best value of $|c_t|$ is $c_t = 0.85^{+0.11}_{-0.12}$.

The graphs in Fig. 5 indicate a tension between the $h \rightarrow \gamma\gamma$ limits and the combined $\kappa_W - \kappa_Z$ and $\kappa_t - \kappa_g$ restrictions in the no-splitting version of our effective Lagrangian. In Sect. 3.3, we will assess if and to what extent this tension can be removed by allowing a_V and a_ρ to become independent.

3.3 Full fit analysis

Assuming that a_V and a_ρ are free independent parameters of the effective Lagrangian under consideration, we calculate
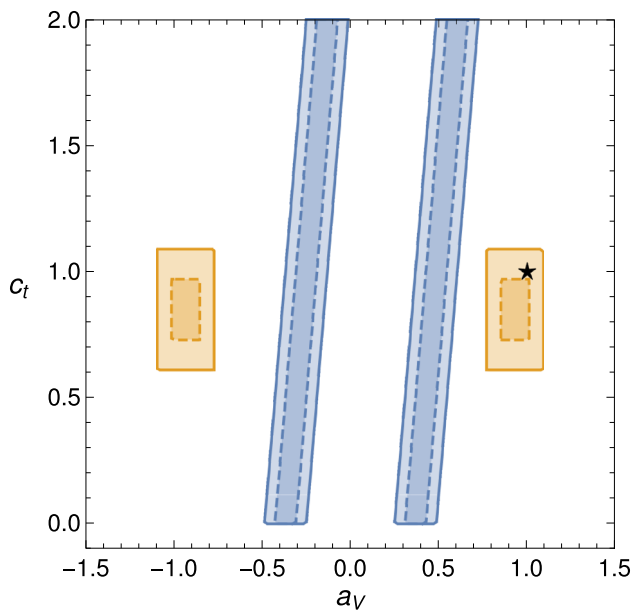
Fig. 5 The 1-sigma (*dashed*) and 2-sigma (*solid*) allowed regions (*blue stripes*) in the $a_V - c_t$ plane derived from the experimental restriction on κ_γ under the no-splitting assumption. The *orange rectangular areas* correspond to the 1-sigma and 2-sigma allowed regions for a_V and c_t obtained by separate fitting of κ_W^2, κ_Z^2 and κ_t^2, κ_g^2, respectively. The *star* indicates the SM values

limits on a_V, a_ρ, and c_t and search for their best values minimizing the χ^2-function built out of the relevant measured observables and their predictions. We use the experimental values of κ_W, κ_Z, κ_t, κ_γ, and κ_g shown in Table 2. Theoretical predictions of the kappas in terms of c_Z, c_W, $c_{\rho\pm}$, and c_t of the Lagrangian interaction term (18) and (5), respectively, are given in (36) and (37). The dependence of c_γ on c_W, $c_{\rho\pm}$, and c_t in (37) is given by (39). The c_Z, c_W, and $c_{\rho\pm}$ are, in turn, related to a_V and a_ρ via (20).

In the interim framework the squares of kappas rather than the kappas themselves are defined and related to measured observables. Therefore, our theoretical predictions are also related to squared kappas and the best fit should be sought for minimizing the following χ^2-function:

$$\chi^2(a_V, a_\rho, c_t) = \left\{ \frac{\kappa_\gamma^2 - [c_\gamma(a_V, a_\rho, c_t)/c_\gamma^{SM}]^2}{\tilde\sigma_\gamma} \right\}^2$$
$$+ \sum_{i=t,g} \left(\frac{\kappa_i^2 - c_t^2}{\tilde\sigma_i} \right)^2$$
$$+ \sum_{i=W,Z} \left[\frac{\kappa_i^2 - c_i^2(a_V, a_\rho)}{\tilde\sigma_i} \right]^2, \quad (45)$$

where $\tilde\sigma_i$'s are the experimental errors for κ_i^2's. The fitting of squares introduces degeneracy of solutions caused by the insensitivity of χ^2 to the relative signs between the kappas and theory parameters. Recall that $c_t > 0$ by assumption.

If we approximate $c_W = c_Z = a_V$ and $c_\rho^\pm = a_\rho$ the Eq. (45) can be simplified without any significant impact on the best-fit values as can be inferred from our conclusions obtained in Sect. 2 (viz., the Eq. (26)). Then, substituting (43) into (45) we obtain

$$\tilde\chi^2(a_V, a_\rho, c_t) = \left[\frac{\kappa_\gamma^2 - (1.28\, a_V + 1.09\, a_\rho - 0.28\, c_t)^2}{2\kappa_\gamma\sigma_\gamma} \right]^2$$
$$+ \left(\frac{\kappa_t^2 - c_t^2}{2\kappa_t\sigma_t} \right)^2 + \left(\frac{\kappa_g^2 - c_t^2}{2\kappa_g\sigma_g} \right)^2$$
$$+ \left(\frac{\kappa_W^2 - a_V^2}{2\kappa_W\sigma_W} \right)^2 + \left(\frac{\kappa_Z^2 - a_V^2}{2\kappa_Z\sigma_Z} \right)^2. \quad (46)$$

It is obvious that $\tilde\chi^2$ has degenerate minima. If the $\tilde\chi^2$-function assumes its minimum value $\tilde\chi^2_{\min}$ for some triplet a_V, a_ρ, c_t then also $\tilde\chi^2(-a_V, -a_\rho, -c_t) = \tilde\chi^2_{\min}$. Nevertheless, by fixing $c_t > 0$ we eliminate half of the degenerate minima.

A simple inspection of the Eq. (46) implies that $\tilde\chi^2$ can be minimized when, at the same time, c_t assumes the value of "weighted average" of κ_t and κ_g, $|a_V|$ assumes a "weighted average" of κ_W and κ_Z, and a_ρ sets to zero the first term with the before-obtained values of c_t and a_V substituted in. Zeroing the first term of (46) amounts to solving a quadratic equation in a_ρ. Thus, there are generally two solutions for (a_V, c_t) and two solutions for $(-a_V, c_t)$, i.e. four solutions in total. Since the first term of Eq. (46) has zero contribution to $\tilde\chi^2_{\min}$ and because the following two terms depend only on c_t and two last terms only on $|a_V|$, all four solutions result in the same value of $\tilde\chi^2_{\min}$.

In particular, by fitting the kappa values of Table 2 we get four minimizing triplets of $\{a_V, a_\rho, c_t\}$ with the same minimal values of $\tilde\chi^2$, $\tilde\chi^2_{\min} = 4.17$. Having d.o.f. $= 5 - 3 = 2$, the value corresponds to the hypothesis backing of 12%. The values of the degenerate best-fit triplets along with the corresponding parameter constraints at 20, 68, and 95% CL are shown in Table 3.

The graphic representation of the best-fit values is depicted in Fig. 6. There, the two-dimensional cut of the $c_t - a_\rho - a_V$ allowed regions by the $c_t = 0.85$ plane is shown. Note that 0.85 is the best-fit value of c_t. The contours depicted in the graph correspond to the 68 and 95% CL regions in the $c_t - a_\rho - a_V$ space. The splitting factors r for the best-fit points A, B, C, and D have the values -0.09, -1.81, -0.56, and -2.27, respectively. The straight line indicates the points of the no-splitting scenario, $a_\rho = a_V$. The full 95% CL region in the $c_t - a_\rho - a_V$ space around the best-fit point A is shown in Fig. 7. The allowed regions around the best-fit points B, C, and D are very similar in shape and size to the region A.

There is a good reason why $a_V a_\rho < 0$ for all four best-fit points. It is because the combined contributions of a_V and

Table 3 The best-fit values of c_t, a_V, and a_ρ corresponding to the four minima of the $\tilde{\chi}^2$-function (46) with the constraints at 20% CL (1-sigma), 68% CL, and 95% CL. All minima (labeled as A, B, C, and D) have the same backing of 12%

| Parameter	A		B		C		D	
c_t								
20% CL		$+0.11$ -0.12		$+0.11$ -0.12		$+0.11$ -0.12		$+0.11$ -0.12
68% CL	0.85	$+0.19$ -0.25	0.85	$+0.19$ -0.25	0.85	$+0.19$ -0.25	0.85	$+0.19$ -0.25
95% CL		$+0.27$ -0.43		$+0.27$ -0.43		$+0.27$ -0.43		$+0.27$ -0.43
a_V								
20% CL		$+0.08$ -0.08		$+0.08$ -0.08		$+0.08$ -0.08		$+0.08$ -0.08
68% CL	0.93	$+0.14$ -0.16	0.93	$+0.14$ -0.16	-0.93	$+0.16$ -0.14	-0.93	$+0.16$ -0.14
95% CL		$+0.20$ -0.25		$+0.20$ -0.25		$+0.25$ -0.20		$+0.25$ -0.20
a_ρ								
20% CL		$+0.16$ -0.17		$+0.17$ -0.15		$+0.17$ -0.16		$+0.16$ -0.17
68% CL	-0.08	$+0.29$ -0.34	-1.68	$+0.34$ -0.28	0.52	$+0.33$ -0.29	2.11	$+0.28$ -0.34
95% CL		$+0.43$ -0.58		$+0.58$ -0.40		$+0.58$ -0.44		$+0.41$ -0.58
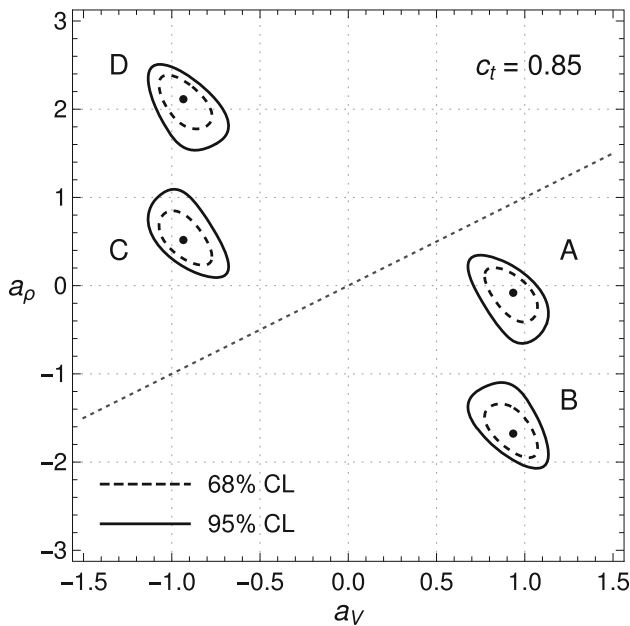
Fig. 6 The two-dimensional cut of the three-dimensional region of the allowed values of parameters a_V, a_ρ, and c_t when c_t is fixed at its best value of 0.85. The *dots* indicate the best-fit values of the fit. They are labeled as *A*, *B*, *C*, and *D* in correspondence with Table 3. The *dashed* and *solid* contours show 68% CL and 95% CL limits. The *straight line* indicates the points of the no-splitting scenario, $a_\rho = a_V$.
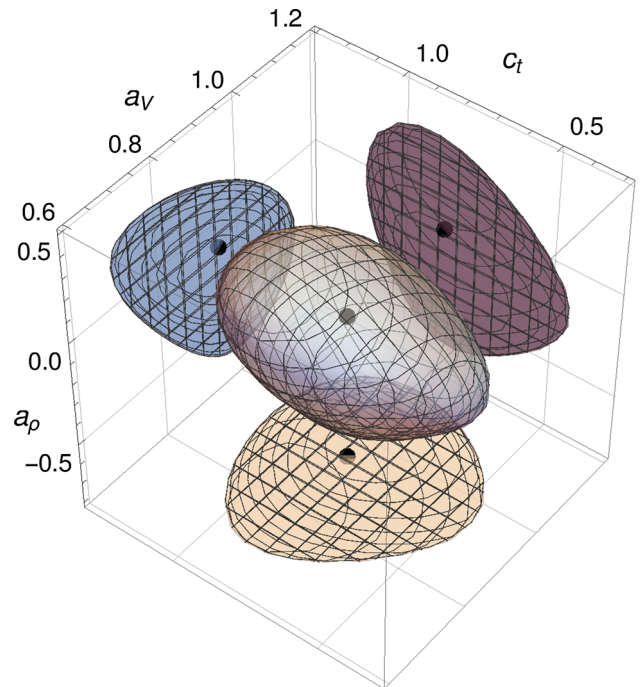
Fig. 7 The 95% CL allowed region of the parameters a_V, a_ρ, and c_t of the $\tilde{\chi}^2$ minima A and the region projections to two-parameter planes. *Dots* indicate the best-fit value and its projections to the planes

c_t to $|c_\gamma|$—the values of a_V and c_t being determined by the other terms of the χ^2-function (46)—overshoot the optimal value of $|c_\gamma|$. Since the a_V contribution dominates the c_t contribution, the a_ρ has to have a sign opposite to the sign of a_V in order to counterbalance the excess. In addition, since we optimize $|c_\gamma|$, rather than c_γ itself, a_ρ resulting in the optimal c_γ plays as well as a_ρ resulting in $-c_\gamma$. Thus, we end up with two a_ρ's for each of the two best-fit values of a_V.

It is not a difficult exercise to impose the no-splitting condition, $a_\rho = a_V$, on $\tilde{\chi}^2$ of (46) in order to obtain a more rigorous quantification and justification of the conclusion we have reached in Sect. 3.2. The fitting of $\tilde{\chi}^2$ results in two minima of unequal depths. This asymmetry results from the sensitivity of $\tilde{\chi}^2$ on the relative sign of a_V and c_t in the κ_γ term. The global minimum assumes the value $\tilde{\chi}^2_{\min} = 21.3$ which for d.o.f. $= 5 - 2 = 3$ corresponds to the hypothesis backing of 0.9%. The minimum resides at $a_V = 0.55 \pm 0.05$ and $c_t = 0.89^{+0.10}_{-0.11}$. The local minimum
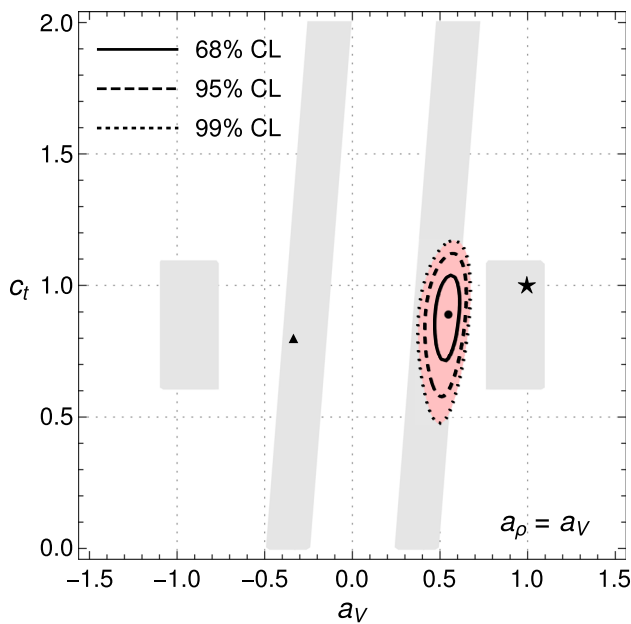
Fig. 8 The fit under the no-splitting condition and the related CL contours. The multiply *encircled red area* corresponds to the allowed regions of 68, 95, and 99% CL. The *dot inside the area* indicates the best-fit value. The *triangle* indicates the position of the second (local) minimum of the χ^2-function. The *star* indicates the SM values of the fitting parameters. For comparison, the graph is interlaced with the reminiscence of Fig. 5 (*gray regions*) where the partial limits obtained by a cruder approach were shown

at $(a_V, c_t) = (-0.33, 0.81)$ amounts to the value higher by $\Delta\tilde{\chi}^2 = 10.7$ above the global minimum.

The fit under the no-splitting condition and the related CL contours are depicted in Fig. 8. Besides, the graph contains reminiscence of Fig. 5 where the limits obtained by the cruder approach of Sect. 3.2 were shown. From a naive visual inspection we would say that the results of the cruder analysis do not contradict the more sophisticated fit performed here. Not only the position of the minimum coincides with the guessed expectation based on Fig. 5, but the obtained hypothesis backing also confirms our qualitative conclusion of Sect. 3.2 about a low support of the data for the no-splitting scenario.

Having the rho-to-Higgs coupling disconnected from the Higgs interactions with the EW gauge bosons and acknowledging that $a_V = c_t = 1$ is compatible with the experiment, one might wonder how successful the parameter a_ρ alone would be in accommodating the existing data if a_V and c_t were kept on their SM values. This simple exercise amounts to minimizing the $\tilde{\chi}^2$-function (46) when $a_V = c_t = 1$. There are two minima, at $a_\rho = -0.12$ and $a_\rho = -1.72$, both with $\chi^2_{\min} = 7$. Since d.o.f. $= 5 - 1 = 4$ our effective Lagrangian with the SM couplings of the Higgs boson to the EW gauge bosons and top quark has 13.8% backing by the data. Raising χ^2 above its minimum by 1 the 1-sigma

(68% CL) constraints read $^{+0.12}_{-0.14}$ and $^{+0.14}_{-0.12}$ for the former and latter a_ρ best values, respectively. Hence, if we had a theoretical reason to demand $a_V = c_t = 1$ the experimental support for the vector triplet of particular a_ρ values would be as good as in the model with loose a_V and c_t.

There are two kappas in the combined ATLAS+CMS measurements [39] not utilized in our analysis: $\kappa_\tau \equiv \Gamma_{\tau^+\tau^-}/\Gamma^{SM}_{\tau^+\tau^-}$ and $\kappa_b \equiv \Gamma_{b\bar{b}}/\Gamma^{SM}_{b\bar{b}}$. In the approximation used in this paper, κ_τ is solely related to c_t, $\kappa_\tau^2 = c_\tau^2$. Thus, it has no impact on the fits of other parameters. Regarding κ_b, while it shares the dependence on c_b with κ_g, its effect on the Higgs production via gluon–gluon fusion is negligible. Consequently, we had dropped the κ_b term from the χ^2-function.

On the other hand, the effective coupling $\kappa_{Z\gamma} \equiv \Gamma_{Z\gamma}/\Gamma^{SM}_{Z\gamma}$ has a similar structure as κ_γ: it depends on a_V, a_ρ, and c_t parameters at leading order. Thus, it has a potential to affect our fits significantly. Unfortunately, the existing measurements restrict $\kappa_{Z\gamma}$ very poorly [42]. Because of that, neither $\kappa_{Z\gamma}$ was included in the χ^2-function (45).

3.4 Unitarity limits for the preferred values of the Higgs couplings

In this Section, we would like to determine how the usability of our phenomenological Lagrangian is restricted by the unitarity limits when the data preferred Higgs couplings obtained in Sect. 3.3 are considered.

Opposite to the SM, our effective Lagrangian is not renormalizable and its applicability is limited to a finite range of energies, not exceeding the point where scattering amplitudes violate unitarity. Considering the low-energy phenomenology of underlying new strong physics it is natural to demand that its successful effective description does not break down below the scale significant to these new interactions. Thus, the results of the investigation of the unitarity limits could be suggestive either of the new physics scale or, in a less fortunate case, of the defects in our Lagrangian. The least we can, and need, to deduce from such an analysis is the range of usability of the effective Lagrangian we play with.

The unitarity of our Lagrangian was investigated in detail in our previous publications [34,35]. Our analysis was based on the scattering amplitudes of the longitudinal EW gauge bosons to the EW gauge bosons. We studied the unitarity of the amplitudes using the Equivalence theorem approximation where the concerned amplitudes were replaced by the pionic scattering amplitudes of the non-linear sigma model. While the approximation corresponds to the limit $g, g' \to 0$ (no pion to EW gauge-boson vertices), the exchange of the Higgs and vector resonances was included.

Even more thorough investigation of the unitarity limits of the same (in relevant sectors) effective Lagrangian was performed in [31]. Beside the elastic $\pi\pi \to \pi\pi$ ampli-

tudes, authors of [31] analyzed the unitarity limits implied by the non-elastic $\pi\pi \to hh$, $\rho_L\rho_L$, $h\rho_L$ processes. Note that wherever applicable the conclusions of [31] coincide with our conclusions [34,35]. In the following, we utilize the findings of these papers for calculation of the tree-level unitarity limits for our Lagrangian. Skipping details of the very standard calculations, below we summarize and discuss the obtained results.

In Fig. 9, we show the $\pi\pi \to \pi\pi$ tree-level unitarity limits.[7] In our case, the $\pi\pi \to \pi\pi$ scattering amplitudes depend only on one of the three Higgs couplings investigated in this paper, namely $|a_V|$. Besides, the amplitudes also depend on M_ρ and g''. There are three graphs in Fig. 9 corresponding to three different masses of the vector resonance: $M_\rho = 1$, 1.5, and 2 TeV. In each graph, there are regions shown where unitarity holds up to $\Lambda = 3$ TeV, 4 TeV, and 5 TeV. The regions are superimposed by the experimentally allowed 2-sigma interval for a_V obtained in Sect. 3.3: $0.77 \leq a_V \leq 1.09$, the best fit being $a_V = 0.93$.

We can see that for the 1 TeV vector resonance unitarity holds up to at least $\Lambda = 3$ TeV when a_V and g'' assumes allowed values,[8] excluding a small region where $g'' \to 12$ and $a_V \to 1.1$. When raising M_ρ, the region where unitarity holds shrinks toward higher g''. At the same time, it slightly shifts toward smaller a_V.

If we dropped the vector resonance from our effective Lagrangian the Higgs resonance alone could unitarize the elastic $\pi\pi$ amplitudes up to some Λ_h that depends on a_V; for example, if a_V assumes its best value of 0.93 the tree-level unitarity holds up to $\Lambda_h = 4.6$ TeV. Perhaps, it might also be worth mentioning that $\Lambda_h \to \infty$ when $a_V = 1$. One wonders how adding the vector triplet to the Higgs-only setup changes the Λ_h limit. To assess it we plot the graph in Fig. 10. There, for given a_V and M_ρ, the values of g'' are divided into two intervals: the one where $\Lambda < \Lambda_h(a_V)$, and the other, where $\Lambda > \Lambda_h(a_V)$. We can see in the graph that if $a_V \geq 1$ adding the vector resonance will always lower the unitarity limit. On the other hand, if $a_V < 1$ there is always g_0'' such that for all $g'' \geq g_0''$ the unitarity limit gets bigger.

In general, the $\pi\pi$ scattering amplitudes are plagued with the linear growths in s. Any added ingredient or assumption that removes the linear growths has a good chance to improve unitarity limits. It can be shown [31] that assuming special relations among the parameters of our Lagrangian (the sum rules) or adding new pseudo-scalar and/or axial-vector fields to our Lagrangian can eliminate the linear terms from the
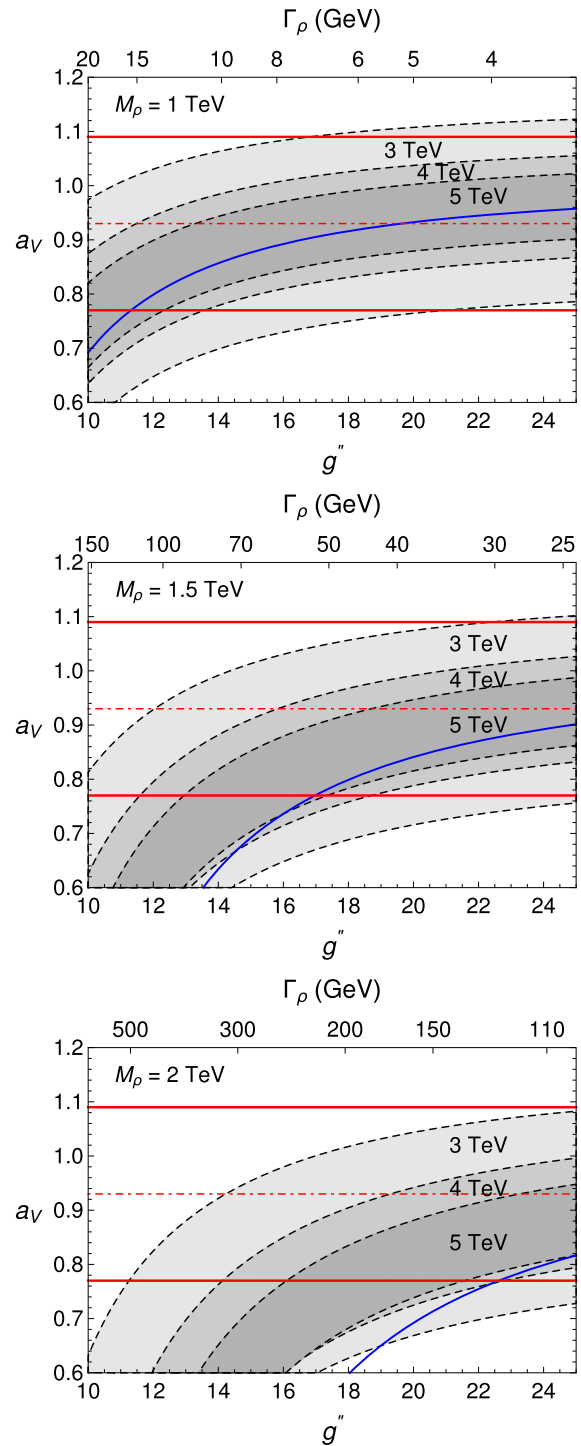
Fig. 9 The tree-level unitarity constraints from $\pi\pi \to \pi\pi$ in the $a_V - g''$ plane for different masses of the vector triplet, $M_\rho = 1$, 1.5, and 2 TeV in the clockwise direction. The *shaded areas* indicate regions where the unitarity holds, up to 3, 4, and 5 TeV. Two horizontal (*solid red*) lines show allowed interval of values of a_V at 2-sigma, the *dot-dashed line* is the best-fit value $a_V = 0.93$. The *blue solid curve* plots the sum rule (47). The *upper axis labels* show the vector resonance decay widths corresponding to g'''s of the *bottom axis*

---

[7] All our calculations use the $\Gamma_\rho = 0$ approximation. This is justifiable as long as M_ρ is far below the unitarity limit in terms of the ρ width.

[8] Recall that $12 \leq g'' \leq 8\pi$.
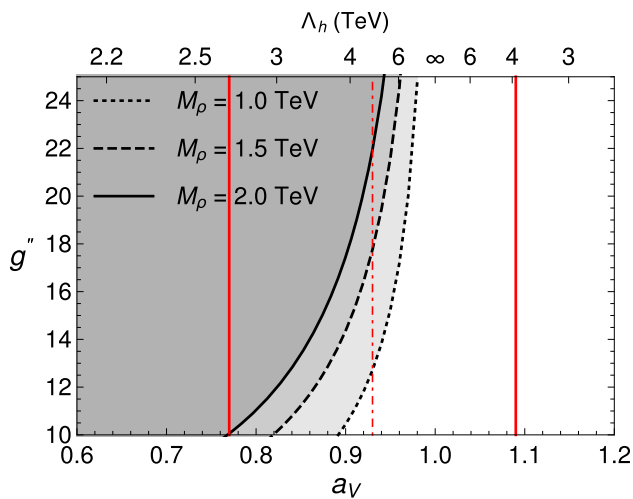
Fig. 10 The regions where the unitarity limit of our model (a_V, g'', M_ρ) gets bigger (*darker area*) and smaller (*lighter area*) than the unitarity limit $\Lambda_h(a_V)$ of the Higgs-only model of a given value a_V. The regions are depicted for three different masses $M_\rho = 1, 1.5$, and 2 TeV. Two *vertical* (*solid red*) *lines* show allowed interval of values of a_V at 2-sigma, the *dot-dashed line* is the best-fit value $a_V = 0.93$

scattering amplitudes. For example, the relation

$$a_V^2 + \frac{3}{4}\alpha = 1 \qquad (47)$$

removes the linear dependence on s from the $\pi\pi \to \pi\pi$ amplitude. The sum rule (47) links a_V with g'' and M_ρ via $\alpha = [2M_\rho/(vg'')]^2$. The resulting sets of (a_V, g'') points for given M_ρ's are also shown in Fig. 9. Obviously, the vector resonance satisfying the existing experimental limits is able to follow the sum rule if its mass stays close or below 1.5 TeV.

It is not possible to satisfy all sum rules resulting from the elastic and inelastic $\pi\pi$ scatterings at the same time [31]. In addition, the sum rule motivated by the $\pi\pi \to h\rho_L$ amplitude reads

$$a_V = a_\rho. \qquad (48)$$

Unfortunately, this is the no-splitting condition not preferred by the data. However, the unitarity-based conclusions reached in [31] rely on the assumption (48). Thus, the results obtained in our analysis call for the investigation of the inelastic unitarity limits when $a_V \neq a_\rho$. However, this is beyond the scope of this paper and currently work in progress.

4 The vector resonance mass limits and the upper bounds on $\sigma(pp \to \rho + X) \times BR$

Undeniably, the search for new vector (and other) resonances has its rightful and important place in the ATLAS and CMS Collaboration's activities. While no discovery has

been made, the direct exclusion limits constantly improve. Unfortunately, the obtained limits are strongly model and parameter dependent. No wonder that the mass exclusion limits found in the literature cover only some of the interesting cases. To the best of our knowledge, there are no exclusion mass limits applicable to the vector resonance of the model studied in this paper.

One of the crucial factors on which the exclusion mass limit depends is the value of the vector resonance gauge coupling g''. As we saw in Fig. 9, in our model, the superposition of the unitarity limits over the experimentally preferred region $0.77 \leq a_V \leq 1.09$ suggests that considering g'' below about 10 is not well justified. We cannot rely on the predictions of our Lagrangian with experimentally allowed values of a_V when $g'' = \mathcal{O}(1)$. This is not of great concern to us if the motivation for our model stems from strongly interacting physics. Independently of this restriction, if we narrowed our considerations to the tBESS interaction pattern of the vector resonance to fermions the low-energy limit from the EW precision measurements reads $g'' \geq 12$ at 95% CL [35]. This is an additional motivation for considering g'' values above 10.

We can evaluate how the existing ATLAS and CMS data restrict our model when we compare the predictions of our model with the upper bounds on the resonance production cross section times its branching ratio for various decay channels. The bounds are rather model independent once spin of the resonance under consideration is specified. Of course, one should keep in mind that the calculations involved proceed under the assumption of a narrow-width resonance.

In Table 4, we present the cross section times branching ratios for various decay channels of the considered model at the LHC collision energy of 13 TeV. The predictions are given for three different values of the resonance masses, namely 1, 1.5, and 2 TeV, and three values of g'', namely 10, 15, and 20. The g'' values were chosen to span the region allowed by the combination of the limits considered and obtained in the previous sections. Note that for $g'' > 20$ our theory not only runs into its perturbativity limit, but heavier vector resonances depart from the narrow-width requirement as can be read off of the upper x-axes of Fig 9.

All model predictions quoted in Table 4 correspond to the scenario when the decay of the vector resonance to fermions is negligible. In the tBESS-like fermion sector, this would correspond to turning off the direct coupling of the vector resonance to the third quark generation,[9] i.e. $b_L = b_R = 0$.

---

[9] In the tBESS model [35], there is no direct interaction of the vector resonance with the light fermions. The direct coupling of the vector resonance to the third quark generation is parameterized by b_L and b_R and by the parameter p which enables the splitting of the direct interactions of the right top and the right bottom quarks. Additional fermion sector parameters $\lambda_{L,R}$ that have been introduced in the tBESS model are, for simplicity, kept at zero values throughout this paper.

Table 4 The production cross section times the branching ratio for different decay channels of the 1, 1.5, and 2 TeV vector resonances of our model considering three different values of g''. The predictions for the ZH and WH channels are given for $a_V = 1$ and $a_\rho = 0$. No direct interactions of the vector resonance with fermions are assumed. The cross sections in the table are calculated for the 13 TeV pp collisions

Channel	g''	$\sigma(\rho^0)$ (pb)	Channel	$\sigma(\rho^+) + \sigma(\rho^-)$ (pb)
WW	10	0.087 0.016 0.005	ZW	0.156 0.030 0.009
	15	0.038 0.007 0.002		0.068 0.013 0.004
	20	0.021 0.004 0.001		0.038 0.007 0.002
ZH	10	$(71\ 2.8\ 0.2) \times 10^{-7}$	WH	$(233\ 9.7\ 0.9) \times 10^{-7}$
	15	$(31\ 1.2\ 0.1) \times 10^{-7}$		$(103\ 4.3\ 0.4) \times 10^{-7}$
	20	$(18\ 0.7\ 0.1) \times 10^{-7}$		$(57\ 2.4\ 0.2) \times 10^{-7}$
$jj\ (u, d, c, s, b)$	10	$(427\ 16.3\ 1.5) \times 10^{-6}$	$jj\ (u, d, c, s)$	$(576\ 23.1\ 2.2) \times 10^{-6}$
	15	$(188\ \ 7.2\ 0.7) \times 10^{-6}$		$(253\ 10.2\ 1.0) \times 10^{-6}$
	20	$(105\ \ 4.0\ 0.4) \times 10^{-6}$		$(142\ \ 5.7\ 0.5) \times 10^{-6}$
$e^+e^- + \mu^+\mu^-$	10	$(107\ 4.1\ 0.4) \times 10^{-6}$	$e\nu_e + \mu\nu_\mu$	$(191\ 7.8\ 0.7) \times 10^{-6}$
	15	$(47\ 1.8\ 0.2) \times 10^{-6}$		$(84\ 3.4\ 0.3) \times 10^{-6}$
	20	$(26\ 1.0\ 0.1) \times 10^{-6}$		$(47\ 1.9\ 0.2) \times 10^{-6}$
tt	10	$(105\ 4.1\ 0.4) \times 10^{-6}$	tb	$(280\ 11.3\ 1.1) \times 10^{-6}$
	15	$(46\ 1.8\ 0.2) \times 10^{-6}$		$(123\ \ 4.9\ 0.5) \times 10^{-6}$
	20	$(26\ 1.0\ 0.1) \times 10^{-6}$		$(69\ \ 2.8\ 0.3) \times 10^{-6}$

Consequently, in this scenario, all fermions can couple to the vector resonance through the mixing-induced interactions only and the decay widths of the neutral/charged vector resonances are dominated by their decays to the EW gauge bosons; $\mathrm{BR}(WW/WZ) > 99\%$.

The experimental upper bounds on the cross section times branching ratio in WW channel read 0.033, 0.012, and 0.005 pb for $M_\rho = 1$, 1.5, and 2 TeV, respectively [43]. This excludes the 1 TeV resonance for $g'' \lesssim 16$ and 1.5 TeV resonance for $g'' \lesssim 12$. The 2 TeV resonance is unrestricted for $g'' \geq 10$. Nevertheless, setting $b_{L,R}$ to their maximally low-energy precision data allowed values—$b_{L,R} \approx 0.1$, as found in [35][10]—can lower $\mathrm{BR}(WW)$ of the 1 TeV resonance down to about 70% for $g'' = 10$, to 30% for $g'' = 15$, and to 12% for $g'' = 20$. In the 2 TeV resonance case, $\mathrm{BR}(WW)$ would be lowered to about 97, 87, and 67%, respectively. Thus, we can see that the fermionic interactions of the vector resonance can noticeably decrease the predictions (and, thus, release the experimental restrictions) of the model in this channel. The same effect can be expected to occur in the ZW channel.

Next, let us compare the predictions of our model to the experimental bounds in the ZW channel. The most restrictive bounds in this channel read 0.051 pb [44], 0.022 pb [44], and 0.009 pb [45] for $M_\rho = 1$, 1.5, and 2 TeV, respectively. This excludes the 1 TeV resonance for $g'' \lesssim 17$ and 1.5 TeV resonance for $g'' \lesssim 12$. Again, the 2 TeV resonance is unre-

stricted for $g'' \geq 10$. In the case of the tBESS-like fermion sector with $b_{L,R} = 0.1$ and $p = 1$, $\mathrm{BR}(WZ)$ gets lowered to about 71, 31, and 12% for $g'' = 10$, 15, and 20, respectively, when $M_\rho = 1$ TeV. When $M_\rho = 2$ TeV, the corresponding BR's read 97, 87, and 67%.

The exclusion limits from the WW/WZ channels mentioned in the previous two paragraphs were obtained from 13.2 fb^{-1} [43,44] and 15.5 fb^{-1} [45] of 13 TeV data. For the sake of completeness, we should mention that the combined $WW + WZ$ analysis of 3.2 fb^{-1} of 13 TeV data [46] implies stronger limits $g'' > 13.6$ and $g'' > 10.6$ for $M_\rho = 1.5$ and 2 TeV, respectively.

At tree level, the ZH and WH decays of the vector resonances occur only when $a_V \neq a_\rho$. In Table 4, we present the predictions of our model for $a_V = 1$ and $a_\rho = 0$. They can be used to derive the predictions for preferred values of a_V and a_ρ that have been found in Sect. 3.3 and quoted in Table 3. Following the formalism introduced in Sect. 2 we find that

$$\Gamma_{ZH/WH}(a_V, a_\rho) = (a_\rho - a_V)^2 \Gamma_{ZH/WH}(1, 0) \qquad (49)$$

Then, taking into account the negligibility of the contributions of Γ_{ZH} and Γ_{WH} to the total decay widths of the neutral and charged resonances, the $(a_\rho - a_V)^2$ scaling applies to the values of the production cross section times the branching ratio for these channels. Thus, when $(a_V, a_\rho) = (0.93, -0.08)$, the numbers in the ZH/WH sector of Table 4 are to be multiplied by 1.02. When $(a_V, a_\rho) = (0.93, -1.68)$, $(-0.93, 0.52)$, or $(-0.93, 2.11)$ the scaling factors are 6.81, 2.10, and 9.24, respectively. The experimental upper limits on the cross section times the branch-

---

[10] While the preferred value of p found in [35] is about 0.25, its statistical preference over any other value of $p \in (0, 1)$ is marginal. Therefore, we consider $p = 1$ in our calculations of the tBESS-like fermion sector contributions, i.e. the same strength of the vector resonance direct couplings to the right top and bottom quarks.

ing ratio are (0.070 [47], 0.032 [47], 0.013 [48]) pb for $M_\rho = (1.0, 1.5, 2.0)$ TeV, respectively, in the ZH channel and (0.12 [47], 0.035 [48], 0.013 [48]) pb in the WH channel. The values predicted in these two channels by our model lie some four orders of magnitude below the experimental upper limits. Thus, the upper limits provide no restriction within the considered range of $g'' \in (10, 20)$.

The same conclusions of no restrictions to our model can also be drawn for the remaining decay channels from which the experimental upper bounds for the production cross section times the branching ratio are available. Namely, the upper bounds for the charged jj channel read 0.210 pb and 0.088 pb for $M_\rho = 1.5$ and 2 TeV, respectively, when 15.7 fb^{-1} of 13 TeV data [49] is processed.[11] The combined neutral+charged jj channel bounds based on 12.9 fb^{-1} of data [50] are 1.20, 0.37, and 0.13 pb for $M_\rho = 1, 1.5,$ and 2 TeV, respectively. The bounds in the $e^+e^- + \mu^+\mu^-$ channel based on 13.3 fb^{-1} of data [51] read 1.30, 0.63, and 0.42 fb for $M_\rho = 1, 1.5,$ and 2 TeV, respectively. The bounds in the $e\nu_e + \mu\nu_\mu$ channel based on 13.3 fb^{-1} of data [52] read 4.8, 1.8, and 1.1 fb for $M_\rho = 1, 1.5,$ and 2 TeV, respectively. The bounds in the tb channel based on 12.9 fb^{-1} of data [53] read 1.8, 0.55, and 0.23 pb for $M_\rho = 1, 1.5,$ and 2 TeV, respectively. Recall that the values in Table 4 correspond to the scenario with no direct fermion interactions with the vector resonance. In the tBESS-like fermion sector the tb channel production would generally be higher.

Finally, there are also the upper bounds for the tt channel based on 3.2 fb^{-1} of data [54]: 1.20, 0.33, and 0.17 pb for $M_\rho = 1, 1.5,$ and 2 TeV, respectively. When we compare these bounds with the predictions in Table 4 we can see that for $g'' \in (10, 20)$ they do not restrict our model. It applies even in the case of the tBESS-like fermion sector with $b_{L,R} = 0.1$ and $p = 1$. Then the predictions in the tt channel will rise to about $10^{-2}, 10^{-3},$ and 10^{-4} pb for $M_\rho = 1, 1.5,$ and 2 TeV, respectively.

5 Conclusions

We have studied the experimental and unitarity limits on the parameters of the strong Higgs sector of the phenomenological Lagrangian where beside the composite 125 GeV Higgs boson the $SU(2)_{L+R}$ triplet of composite vector resonances is explicitly present. The ESB sector of our effective Lagrangian has been based on the $SU(2)_L \times SU(2)_R \to SU(2)_{L+R}$ non-linear sigma model while the scalar resonance has been introduced as the $SU(2)_{L+R}$ singlet. The vector resonance has been built in employing the hidden local symmetry approach.

For the interactions of the Higgs boson with the EW gauge fields, the vector triplet, and the top quark the assumed symmetries allow one to introduce three free independent modification factors, a_V, a_ρ, and c_t. After the transformation from the flavor to mass gauge-boson eigenstate basis, the first two factors combine into modifiers c_Z, c_W, c_{ρ^0}, $c_{\rho^\pm}$, $c_{Z\rho^0}$, and $c_{W\rho^\pm}$ of the vertices hZZ, hW^+W^-, $h\rho^0\rho^0$, $h\rho^\pm\rho^\pm$, $hZ\rho^0$, and $hW^\pm\rho^\mp$, respectively. If $r = a_\rho/a_V \neq 1$, then c_Z differs from c_W. Nevertheless, for quite a large interval of r's around one, e.g., $|r| \leq 3$, the effect is very small. The corrections to the custodial symmetry protected rho parameter induced by the differing a_V and a_ρ are negligible and well within the experimental limits. For many phenomenological considerations, the approximations $c_Z = c_W = a_V$, $c_{\rho^0} = c_{\rho^\pm} = a_\rho$, and $c_{Z\rho^0} = c_{W\rho^\pm} = 0$ are satisfactory over quite a large region of r values and for all relevant values of g'' and M_ρ.

The limits on the free Higgs coupling factors $a_V, a_\rho,$ and c_t have been calculated using constraints on the kappa parameters of the interim framework. The constraints were obtained in the recent ATLAS+CMS Collaborations analysis of various Higgs-related processes based on data from 2011 and 2012. We have used the fitting scenario where no non-SM decays of the Higgs is assumed and where the branching ratio of invisible and/or undetected decay products is zero. In addition, new particles in loops are allowed. Out of seven free parameters in this scenario—loop-level κ_g, κ_γ, and tree-level $\kappa_W, \kappa_Z, \kappa_t, \kappa_b, \kappa_\tau$—we have used all but the last two to find the restrictions on $a_V, a_\rho,$ and c_t; κ_b and κ_τ have been ignored because their impact on the fitting parameters was negligible.

By fitting the kappas we have established that the simple case of $a_\rho = a_V$ is strongly disfavored by the data. There are four triplets of the best-fit values of $a_V, a_\rho,$ and c_t that can satisfy the fitted data. Namely, $(a_V, a_\rho, c_t) = (0.93, -0.08, 0.85),$ $(0.93, -1.68, 0.85),$ $(-0.93, 0.52, 0.85),$ and $(-0.93, 2.11, 0.85)$. The 1-sigma deviation (i.e., $\chi^2_{\min} + 1$) for a_V at all four best values is the same: ± 0.08. It also applies to c_t. Its 1-sigma errors read $^{+0.11}_{-0.12}$ for each best value of c_t. As far as a_ρ is concerned its 1-sigma deviations differ slightly at each of the best-fit values. However, overall they do not exceed ± 0.17. The hypothesis backing for all four fits is the same and amounts to 12%. The tied score might be tilted in favor of one of the fits once $\kappa_{Z\gamma}$ gets measured more precisely.

Using scattering amplitudes of the longitudinal EW gauge bosons in the Equivalence theorem approximation we have studied the restrictions of the usability of our phenomenological Lagrangian imposed by the unitarity limits when the data preferred Higgs couplings obtained in this paper are considered. We have found from the $\pi\pi \to \pi\pi$ scattering that for $M_\rho = 1$ TeV unitarity holds up to at least $\Lambda = 3$ TeV when $0.77 \leq a_V \leq 1.09$ and $12 \leq g'' \leq 25$. As M_ρ grows

---

[11] The quoted upper bounds for all jj channels include an acceptance factor.

the region where unitarity holds shrinks toward higher g'' and lower a_V. Even if $M_\rho = 2$ TeV, the considered model is well below the unitarity limit at significant portions of the experimentally allowed region of a_V. Nevertheless, these conclusions should be complemented by a similar analysis of the $\pi\pi$ scattering with h and ρ_L in the final state where a_V and a_ρ would be independent parameters, thus allowing also for $a_V \neq a_\rho$ preferred by the data.

Our calculations show that the masses in the range 1 TeV $\leq M_\rho \leq 2$ TeV are not excluded in parts or even full parameter space of our theory. When the model's predictions face the upper bounds on the production cross section times branching ratio in different decay channels the 1 TeV resonance gets excluded in the WW channel when $g'' \gtrsim 16$ and in the WZ channel when $g'' \gtrsim 17$. Both, the WW and WZ channel measurements exclude the 1.5 TeV resonance when $g'' \gtrsim 14$. These restriction can get weakened once the direct interactions of the vector resonance with the fermion sector are introduced. None of the other reviewed decay channels excludes our model, at least when $10 \leq g'' \leq 20$.

In the view of the results obtained in this paper we would conclude that even such a simplistic effective description of possible early phenomenology of strong BSM physics as the one studied here is capable to accommodate the existing data.

Appendix: Some definitions

In this appendix, we show definitions of some of the quantities used in Sect. 2 to express the parts of our phenomenological Lagrangian relevant to this paper. All details regarding the Lagrangian structure and how it was built can be found in [34,35].

The field strength tensors of the $SU(2)_L \times U(1)_Y \times SU(2)_{\text{HLS}}$ gauge fields are defined as

$$\boldsymbol{W}_{\mu\nu} = \partial_\mu \boldsymbol{W}_\nu - \partial_\nu \boldsymbol{W}_\mu + [\boldsymbol{W}_\mu \boldsymbol{W}_\nu], \tag{A.1}$$

$$\boldsymbol{B}_{\mu\nu} = \partial_\mu \boldsymbol{B}_\nu - \partial_\nu \boldsymbol{B}_\mu, \tag{A.2}$$

$$\boldsymbol{V}_{\mu\nu} = \partial_\mu \boldsymbol{V}_\nu - \partial_\nu \boldsymbol{V}_\mu + [\boldsymbol{V}_\mu \boldsymbol{V}_\nu], \tag{A.3}$$

where $\boldsymbol{W}_\mu = ig W_\mu^a \tau^a$, $\boldsymbol{B}_\mu = ig' B_\mu \tau^3$, and $\boldsymbol{V}_\mu = i\frac{g''}{2} V_\mu^a \tau^a$ with the gauge couplings g, g', and g'', respectively.

The ESB sector contains six unphysical real scalar fields, would-be Goldstone bosons of the model's spontaneous symmetry breaking. The six real scalar fields $\varphi_L^a(x), \varphi_R^a(x)$, $a = 1, 2, 3$, are introduced as parameters of the $SU(2)_L \times SU(2)_R$ group elements in the exp-form $\xi(\boldsymbol{\varphi}_{L,R}) = \exp(i\boldsymbol{\varphi}_{L,R}\boldsymbol{\tau}/v) \in SU(2)_{L,R}$ where $\boldsymbol{\varphi} = (\varphi^1, \varphi^2, \varphi^3)$. The quantities $\bar{\omega}_\mu^\parallel$ and $\bar{\omega}_\mu^\perp$ are, respectively, the $SU(2)_{L-R}$ and $SU(2)_{L+R}$ projections of the gauged Maurer–Cartan 1-form,

$$\bar{\omega}_\mu^\parallel = \omega_\mu^\parallel + \frac{1}{2}\left(\xi_L^\dagger \boldsymbol{W}_\mu \xi_L + \xi_R^\dagger \boldsymbol{B}_\mu \xi_R\right) - \boldsymbol{V}_\mu, \tag{A.4}$$

$$\bar{\omega}_\mu^\perp = \omega_\mu^\perp + \frac{1}{2}\left(\xi_L^\dagger \boldsymbol{W}_\mu \xi_L - \xi_R^\dagger \boldsymbol{B}_\mu \xi_R\right), \tag{A.5}$$

where $\omega_\mu^{\parallel,\perp} = (\xi_L^\dagger \partial_\mu \xi_L \pm \xi_R^\dagger \partial_\mu \xi_R)/2$.

References

1. G. Aad et al., ATLAS Collaboration. Phys. Lett. B **716**, 1 (2012)
2. S. Chatrchyan et al., CMS Collaboration. Phys. Lett. B **716**, 30 (2012)
3. R. Barbieri, B. Bellazzini, V.S. Rychkov, A. Varagnolo, Phys. Rev. D **76**, 115008 (2007)
4. C. Csaki, A. Falkowski, A. Weiler, JHEP **0809**, 008 (2008)
5. R. Contino. arXiv:1005.4269 [hep-ph]
6. R. Contino, D. Marzocca, D. Pappadopulo, R. Rattazzi, JHEP **1110**, 081 (2011)
7. A. Pomarol, F. Riva, JHEP **1208**, 135 (2012)
8. D. Pappadopulo, A. Thamm, R. Torre, JHEP **1307**, 058 (2013)
9. M. Montull, F. Riva, E. Salvioni, R. Torre, Phys. Rev. D **88**, 095006 (2013)
10. G. Panico, A. Wulzer, Lect. Notes Phys. **913**, 1 (2016). arXiv:1506.01961
11. W.A. Bardeen, C.T. Hill, M. Lindner, Phys. Rev. D **41**, 1647 (1990)
12. G.F. Giudice, C. Grojean, A. Pomarol, R. Rattazzi, JHEP **0706**, 045 (2007)
13. R. Foadi, M.T. Frandsen, T.A. Ryttov, F. Sannino, Phys. Rev. D **76**, 055005 (2007)
14. T.A. Ryttov, F. Sannino, Phys. Rev. D **78**, 115010 (2008)
15. F. Sannino, Acta Phys. Polon. B **40**, 3533 (2009)
16. A.R. Zerwekh, Mod. Phys. Lett. A **25**, 423 (2010)
17. A.E. Cárcamo Hernández, R. Torre, Nucl. Phys. B **841**, 188 (2010)
18. G. Burdman, C.E.F. Haluch, JHEP **1112**, 038 (2011)
19. T. Hapola, F. Sannino, Mod. Phys. Lett. A **26**, 2313 (2011)
20. A.E. Cárcamo Hernández, C.O. Dib, N. Neill, A.R. Zerwekh, JHEP **1202**, 132 (2012)
21. R. Foadi, M.T. Frandsen, F. Sannino, Phys. Rev. D **87**, 095001 (2013)
22. R. Contino, M. Ghezzi, C. Grojean, M. Muhlleitner, M. Spira, JHEP **1307**, 035 (2013)
23. O. Castillo-Felisola, C. Corral, M. González, G. Moreno, N.A. Neill, F. Rojas, J. Zamora, A.R. Zerwekh, Eur. Phys. J. C **73**, 2669 (2013)
24. A.E. Cárcamo Hernández, C.O. Dib, A. R. Zerwekh, Eur. Phys. J. C **74**, 2822 (2014)

25. A.E. Cárcamo Hernández, C.O. Dib, A. R. Zerwekh, Nucl. Part. Phys. Proc. **35**, 267–269 (2015)
26. D. Pappadopulo, A. Thamm, R. Torre, A. Wulzer, JHEP **1409**, 060 (2014)
27. A. Belyaev, M.S. Brown, R. Foadi, M.T. Frandsen, Phys. Rev. D **90**, 035012 (2014)
28. B.W. Lee, C. Quigg, H.B. Thacker, Phys. Rev. D **16**, 1519 (1977)
29. B.W. Lee, C. Quigg, H.B. Thacker, Phys. Rev. Lett. **38**, 883 (1977)
30. M.S. Chanowitz, M.K. Gaillard, Nucl. Phys. B **261**, 379 (1985)
31. B. Bellazzini et al., JHEP **11**, 003 (2012)
32. M. Bando, T. Kugo, K. Yamawaki, Phys. Rep. **164**, 217 (1988)
33. R.S. Chivukula et al., Phys. Rev. D **74**, 075011 (2006)
34. M. Gintner, J. Juráň, I. Melo, Phys. Rev. D **84**, 035013 (2011)
35. M. Gintner, J. Juráň, Eur. Phys. J. C **73**, 2577 (2013)
36. R. Casalbuoni, S. De Curtis, D. Dominici, R. Gatto, Phys. Lett. **155B**, 95 (1985)
37. R. Casalbuoni, S. De Curtis, D. Dominici, R. Gatto, Nucl. Phys. B **282**, 235 (1987)
38. R. Casalbuoni, P. Chiappetta, S. De Curtis, F. Feruglio, R. Gatto, B. Mele, J. Terron, Phys. Lett. B **249**, 130 (1990)
39. The ATLAS and CMS Collaborations. arXiv:1606.02266
40. The LHC Higgs Cross Section Working Group. arXiv:1307.1347
41. The LHC Higgs Cross Section Working Group. arXiv:1101.0593
42. ATLAS Collaboration, Eur. Phys. J. C **76**, 6 (2016)
43. ATLAS Collaboration, ATLAS-CONF-2016-062
44. ATLAS Collaboration, ATLAS-CONF-2016-082
45. ATLAS Collaboration, ATLAS-CONF-2016-055
46. ATLAS Collaboration. arXiv:1606.04833
47. ATLAS Collaboration. arXiv:1607.05621
48. ATLAS Collaboration, ATLAS-CONF-2016-083
49. ATLAS Collaboration, ATLAS-CONF-2016-069
50. CMS Collaboration, CMS-PAS-EXO-16-032
51. ATLAS Collaboration, ATLAS-CONF-2016-045
52. ATLAS Collaboration, ATLAS-CONF-2016-061
53. CMS Collaboration, CMS-PAS-B2G-16-017
54. ATLAS Collaboration, ATLAS-CONF-2016-014